

1           **Comparative study of tectonic tremor locations: characterization of slow**  
2           **earthquakes in Guerrero, Mexico**

3 **J. Maury<sup>1</sup>, S. Ide<sup>1</sup>, V.M. Cruz-Atienza<sup>2</sup>, V. Kostoglodov<sup>2</sup>, G. González-Molina<sup>2</sup> and X.**  
4 **Pérez-Campos<sup>2</sup>**

5 <sup>1</sup>Earth and Planetary Science, University of Tokyo, Tokyo, Japan.

6 <sup>2</sup>Instituto de Geofísica, Universidad Nacional Autónoma de México, Mexico City, Mexico.

7 Corresponding author: Julie Maury ([maury@eps.s.u-tokyo.ac.jp](mailto:maury@eps.s.u-tokyo.ac.jp))

8 **Key Points:**

- 9       • Two seismic networks provide tremor catalogs with different resolutions.
- 10      • Moment tensors of slow earthquakes in Guerrero are consistent with plate motion.
- 11      • Matched filtering detected eleven VLF events accompanying tremors.
- 12

## 13 Abstract

14 Deep tectonic tremor in Guerrero, Mexico, has been observed using dense temporal seismic  
15 networks (i.e., the Meso-American Subduction Experiment and Guerrero Gap Experiment, G-  
16 GAP, arrays) during two different time periods. We apply a set of seismic waveform analysis  
17 methods to these datasets to constrain the locations of tremors and determine the associated  
18 moment tensors. First we detect and locate the tremors. Next, very low frequency (VLF) signals  
19 are identified by stacking waveform data during tremor bursts, and their moment tensors are  
20 determined. Finally, to better investigate the link between tremors and VLF earthquakes, we  
21 detect VLF events using a matched filtering algorithm to search continuous seismic records.  
22 None of the 11 VLF events detected by this method occurred in the absence of tremor bursts  
23 suggesting they are indeed part of the same phenomena. Unlike previous investigations, our  
24 results for the G-GAP period reveal that downdip tremor activity (i.e., in the so-called “sweet  
25 spot”) is segmented into two patches separated by 40 km in the along-trench direction, indicating  
26 possible variations in the geometry of the plate interface and/or slab effective pressure. Moment  
27 tensors of VLF signals are consistent with shear slip on the near-horizontal plate interface, but  
28 source depths are about 5 km deeper than the established plate interface. The slip directions of  
29 the VLF events are slightly ( $\sim 10^\circ$ ) counterclockwise of the plate convergence direction,  
30 indicating that strain energy promoting left-lateral strike-slip motion may accumulate in the  
31 continental crust during the inter-seismic period.

## 32 1 Introduction

33 Deep tectonic tremors that accompany slow slip events (SSEs) were discovered almost  
34 simultaneously in two regions: Cascadia [Rogers and Dragert, 2003] and Japan [Obara, 2002].  
35 Later, Shelly *et al.* [2007], when studying low frequency earthquakes (LFEs), proposed that non-  
36 volcanic tremors, or tectonic tremors observed between 1 and 15 Hz, could be merely a  
37 superposition of LFEs. Very low frequency (VLF) earthquakes detected in the 0.02–0.05 Hz  
38 frequency band present intermediary duration scale between tremors, LFEs, and SSEs, with  
39 durations between days and years [Ito *et al.*, 2007]. Many more recent studies have investigated  
40 the characteristics of these signals [Schwartz and Rokosky, 2007; Peng and Gomberg, 2010;  
41 Beroza and Ide, 2011]. Slow earthquakes consist of long-duration deformation signals with low-  
42 amplitude seismic waves. One of their distinguishing characteristics is that their seismic  
43 moments scale with their durations, contrary to fast earthquakes seismic moments that scale with  
44 their cubic durations [Ide *et al.*, 2007a]. Much remains to be understood about slow earthquakes  
45 and the relationships among the different types of events. For example, why, with comparable  
46 networks, are only SSEs and VLF earthquakes found in some places (e.g., Boso), while in other  
47 region (e.g., Nankai), all known types of slow earthquakes are present [Beroza and Ide, 2011]?  
48 Do slow earthquakes occur in every subduction zone? To answer these questions, and better  
49 characterize slow earthquakes, studies of different subduction zones are needed.

50 Locating tremors is not easy because there are no clear P or S arrivals. Various methods  
51 have been implemented to circumvent this problem: the better-known examples include envelope  
52 correlation [Obara, 2002; Ide, 2010], source scanning algorithms [Kao *et al.*, 2005], the use of  
53 differential P and S arrival times [La Rocca *et al.*, 2009], LFE detection [Shelly *et al.*, 2007;  
54 Brown *et al.*, 2008], and tremor energy and polarization methods [Cruz-Atienza *et al.*, 2015].  
55 Most of these methods have been successfully applied in Cascadia and Japan because of the  
56 availability of well-distributed seismological networks. Along with other techniques, they have

57 been subsequently applied to other subduction zones in locations such as Mexico [Payero *et al.*,  
58 2008; Husker *et al.*, 2012], Costa Rica [Brown *et al.*, 2009], and Taiwan [Peng and Chao, 2008],  
59 as well as transform faults in California [Nadeau and Dolenc, 2005]. In some places (Nankai,  
60 Cascadia), tremors occur in the same areas as SSEs [Obara *et al.*, 2004; Brudzinski and Allen,  
61 2007], while in others (Mexico, Costa Rica, New Zealand) they are located slightly apart from  
62 each other [Kostoglodov *et al.*, 2010; Outerbridge *et al.*, 2010; Ide, 2012]. Thus, we wonder how  
63 sparser station networks impact tremor detection and location. Assessing the robustness of these  
64 locations, and the corresponding location techniques, is a key goal of this study.

65 Once the locations of slow earthquakes are known, we need to consider what their  
66 mechanisms are, and whether they are the same for all classes of slow earthquakes. It has been  
67 suggested that deep tectonic tremors occur as a result of shear slip on the plate interface [Wech  
68 and Creager, 2007; Ghosh *et al.*, 2009; Cruz-Atienza *et al.*, 2015]. However, since tremor  
69 signals are extremely emergent, it is difficult to constrain their moment tensors and their vertical  
70 location very precisely. Shelly *et al.* [2007] demonstrated that tremors are composed of LFEs  
71 swarms, meaning that complete focal mechanism solutions can be obtained for individual LFEs  
72 [Ide *et al.*, 2007b]. These LFEs have been clearly located on the plate interface [Shelly *et al.*,  
73 2006; Brown *et al.*, 2009]. Focal mechanisms have then been determined for LFEs in Cascadia  
74 [Royer and Bostock, 2014], Nankai [Imanishi *et al.*, 2016], and Mexico [Frank *et al.*, 2013].  
75 Focal mechanisms for VLF events have also been determined for isolated events in the Nankai  
76 [Ito *et al.*, 2007, 2009] and Ryukyu subduction zones [Ando *et al.*, 2012]. More recently, Ide and  
77 Yabe [2014] used a stacking method to detect VLF events occurring simultaneously with  
78 tremors, and determined their corresponding focal mechanisms, with results that corroborate the  
79 hypothesis that slow earthquakes all arise from the same physical phenomena. However, focal  
80 mechanisms must be resolved for tremor samples from other locations before such general  
81 conclusions can be accepted.

82 This study focuses on the Guerrero region of Mexico, where the Cocos plate is  
83 subducting beneath the North American plate at the Middle America Trench (MAT). Many  
84 subduction thrust earthquakes have occurred along the Mexican coast with a recurrence time of  
85 30–60 years except in the so-called “Guerrero Gap”, where the most recent  $M_w \sim 7.5$  earthquake  
86 in the region occurred in 1911. Every four years, long-term SSEs occur down-dip of the Guerrero  
87 Gap seismogenic interface (Figure 1 a), with a total moment magnitude of 7.5, making these the  
88 largest SSEs detected to date in subduction zones [e.g., Kostoglodov *et al.*, 2003; Iglesias *et al.*,  
89 2004; Larson *et al.*, 2007; Radiguet *et al.*, 2012]. These are thought to enable the aseismic  
90 release of most of the strain energy that accumulates in the seismogenic zone [Radiguet *et al.*,  
91 2012]. Tectonic tremors have also been detected down-dip of the SSEs [Payero *et al.*, 2008],  
92 occurring over a wide area and separated into two patches in the subduction direction [Husker *et al.*  
93 *et al.*, 2012; Cruz-Atienza *et al.*, 2015], a feature that is uncommon in other subduction zones. The  
94 up-dip tremor patch is active mainly during the long-term SSEs, while the down-dip patch, often  
95 called the “sweet spot” [Husker *et al.*, 2012], is active almost continuously. Detections of LFEs  
96 support these findings and suggest that short-term SSEs down-dip of long-term ones could be  
97 related to this second tremor patch [Frank *et al.*, 2014, 2015]. Another unique characteristic of  
98 Guerrero is that the subduction interface is sub-horizontal for nearly 200 km (Figure 1). Slow  
99 earthquakes occur predominantly in this flat part of the subducting slab.

100 This study has two main aims. First, we compare tremor locations obtained from two  
101 temporal networks with very different spatial configurations. Second, we determine the moment

102 tensors of tremors using stacked waves in the VLF band, as has been done in Japan [*Ide and*  
103 *Yabe, 2014*] and Taiwan [*Ide et al., 2015*]. This provides a vastly more complete picture of the  
104 tremor source mechanism in Guerrero, since previous studies have resolved only rake directions  
105 [*Cruz-Atienza et al., 2015*], with one complete focal mechanism estimated for the entire area  
106 [*Frank et al., 2013*]. In addition, we search for individual VLF events using a matched filtering  
107 algorithm, to determine the temporal correlation (if any) between VLF events and tremors.

## 108 **2 Seismic data**

109 We analyze slow earthquakes in Guerrero in two time periods between 2005 and 2012,  
110 corresponding to two different temporary network deployments. During these time periods, two  
111 analyses are performed: tremors are located and moment tensors of stacked VLF signals are  
112 determined. For high-frequency tremor detection, every available station is used. Moment tensor  
113 calculations in the VLF band (0.02–0.05 Hz) use only data from broadband sensors.

114 During the first time period, from January 2005 to June 2007, the data analyzed are from  
115 broadband sensors deployed during the Meso-American Subduction Experiment (MASE)  
116 [*MASE, 2007*]. For the tremor locations, 29 of 100 network stations are selected, based on their  
117 proximity to the region of interest. For moment tensor determination, 17 sensors are selected,  
118 based on their relatively high signal-to-noise ratios in the VLF band. Since the original purpose  
119 of the MASE project was a structural survey, all seismometers were deployed in a linear  
120 configuration almost perpendicular to the trench (Figure 1).

121 During the second time period, from November 2009 to mid-2012, seismograms from 35  
122 vertical-component short-period sensors and 3 medium-period three-component sensors from the  
123 G-GAP experiment are used for tremor location. These instruments are localized around the  
124 “sweet spot”; each red circle in Figure 1 corresponds to a mini-array with six sensors separated  
125 by less than 1 km.

126 In addition, broadband seismic data from the permanent network of the Servicio  
127 Seismológico Nacional (SSN) are used for both analyses. Two permanent stations, ARIG and  
128 TLIG, were added between the two temporary deployments, located on either side of the “sweet  
129 spot” (Figure 1), thereby improving the network coverage for the second study. Tremor  
130 detectability and focal mechanism reliability changed with time due to this varying stations  
131 availability (Figure 2 e). During the first time period, the network is linear but consists of  
132 broadband stations; during the second time period, the network provides good azimuthal  
133 coverage around the sweet spot, but has few broadband stations. Assuming that the tremor  
134 signals are mainly SH-waves, horizontal components should be used. However, the G-GAP  
135 temporary network is composed primarily of vertical-component sensors; thus, for the second  
136 time period, vertical components are used for sensors with no horizontal component (35 of 38  
137 stations).

## 138 **3 Methods**

139 To detect and locate tremors, we use 34 stations from the first time period and 45 stations  
140 from the second. We apply an envelope correlation method [*Obara, 2002; Ide, 2010*] to detect  
141 the events. The signals are band-passed between 2 and 8 Hz, squared, low-pass filtered at 0.2 Hz,  
142 and resampled at 1 sample per second. The envelope is approximated as the square root of the  
143 resampled data, following *Ide* [2010]. We use 5 minute time windows with 2.5 min of overlap  
144 between successive calculations. A detection is declared when at least eight normalized cross-

145 correlations reach the threshold value of 0.6. For the G-GAP time period, correlations between  
 146 stations within the same mini-arrays are not considered. To locate the detected tremors, we solve  
 147 a nonlinear inverse problem that minimizes the squared misfit between observed and calculated  
 148 travel times [Ide, 2010]. A velocity model obtained from S wave tomography by Iglesias *et al.*  
 149 [2010] is used for location, completed by the AK135 1D velocity model [Kennett *et al.*, 1995]  
 150 for the deeper part. A clustering technique is applied to reject outliers and false detections: only  
 151 events that are within a space–time window of 10 km and 1 day with at least one other event are  
 152 kept. Moreover, events at latitudes less than 17.35° are rejected, because most of these events are  
 153 earthquakes.

154 In addition, to confirm our tremor locations, we also apply the Tremor Energy and  
 155 Polarization (TREP) method [Cruz-Atienza *et al.*, 2015] to locate tremor sources using the G-  
 156 GAP array. Given tremor detections by means of a spectral threshold strategy [Husker *et al.*,  
 157 2010], the TREP method simultaneously determines the locations and rake angles of double-  
 158 couple tremor sources that explain both the spatial distribution of energy (in all three  
 159 components) and the azimuth of the particle motion polarization ellipsoid. A grid search is  
 160 performed in a 3D regular lattice below the array. For each node of the lattice, a time scan is  
 161 performed using 1 min moving windows with 20 s overlap.

162 Since moment tensors of tremors are difficult to estimate, we next attempt to identify  
 163 VLF signals and invert these for their moment tensors. A grid of reference points, separated by  
 164 11 km in the strike-parallel and strike-perpendicular directions, is prepared for the tremor  
 165 centroid region. Seismograms are stacked at the time of occurrence for all tremors within 10 km  
 166 of a reference point. If the number of tremors exceeds 100 (200 for the G-GAP time period), they  
 167 are stacked in the VLF band; note that a larger number of tremors is needed for G-GAP time  
 168 period because fewer stations are available. The relative amplitude of the stacked signal at the  $j$ -  
 169 th station is given by

$$170 \quad u_j^s(t) = \frac{\sum_i u_{ij}(t)/A_i}{\sum_i 1/A_i}, \quad (1)$$

171 where  $u_{ij}(t)$  is the velocity from the  $i$ -th tremor at the  $j$ -th station and  $A_i$  represents the relative  
 172 amplitude of the  $i$ -th event determined during an outlier control procedure. For further details,  
 173 see Ide and Yabe [2014]. Once these signals are stacked, we estimate their deviatoric moment  
 174 tensor with five basis vectors  $M_i$ , by assuming that the stacked velocity can be expressed as

$$175 \quad u_j^s(t) = \sum g_{ij}(t)M_i + e_j(t)/W_j; \quad (2)$$

176 where  $g_{ij}$  is the theoretical waveform for a unit source of the  $i$ -th moment tensor component,  $e_j$  is  
 177 the Gaussian-distributed error, and  $W_j$  is a weighting factor. The velocity structure used for  
 178 tremor detection is also used for estimating  $g_{ij}$ . The weighting factor corresponds to the inverse  
 179 of the maximum amplitude of the noise in a 400 s time window before the event. Components  
 180 with a noise level higher than 10 times the lowest noise level are not used. The best solution is  
 181 obtained by maximizing the variance reduction,

$$182 \quad s(\mathbf{M}) = \frac{VR=1-s(\mathbf{M})/s(0)}{\|W_j u_j^s(t) - \sum_i W_j g_{ji}(t)M_i\|^2} \quad (3)$$

183 as a function of depth and source duration.

184 We do not try to retrieve the isotropic component of the moment tensor, because we do not have  
 185 sufficient resolution. However, we consider this component small, as is the case for well-  
 186 constrained VLF moment tensors in Japan [Ide and Yabe, 2014]. During the MASE time period,

187 the network is linear, and therefore cannot adequately constrain some parts of the moment tensor.  
188 During the G-GAP time period, only seven stations are available, with five of these aligned, also  
189 limiting the resolution.

#### 190 **4 Tremor location**

191 A total of 2990 tremors are detected during the first time period (MASE, 29 months), and  
192 5317 tremors during the second (G-GAP, 32 months). The higher number of detections during  
193 the G-GAP time period is due to the longer time period and more optimal array geometry.

194 Figure 2 shows the tremor locations obtained for both time periods. Even if the extent of  
195 the locations is similar, the distributions of tremor locations differ considerably between the two  
196 datasets. Using the MASE data, the two clusters already identified by *Husker et al.* [2012] and  
197 defined by *Frank et al.* [2014] are clearly visible: updip in the transient zone, and downdip in the  
198 sweet spot. The G-GAP time period gives more details on the sweet spot, which appears to  
199 constitute two distinct locations in the along-strike direction, separated by ~40 km (the distance  
200 between the locations of the maximum number of tremors in each cluster). These two clusters are  
201 elongate in the dip direction, and extend beyond the distributions determined using MASE time  
202 period data. The depth of the tremors is the least well-constrained parameter, as is apparent from  
203 the wide range of results obtained (Figure 2 **a** and **c**). However, the mean depth is 38 with a  
204 standard deviation of  $\pm 11$  km for both datasets, which falls within the range reported in previous  
205 studies [*Frank et al.*, 2014; *Cruz-Atienza et al.*, 2015]. An apparent east–west depth trend is  
206 observable in the MASE locations, with tremors located deeper in the western part of the cluster  
207 (Figure 2 **c**, blue circles). This trend is probably an artifact linked to the network configuration.

208 The standard deviations of the model covariance matrix, calculated for the estimated  
209 parameters (Figure 3), characterize the location errors. While the errors in latitude are  
210 comparable for both time periods, the errors in longitude are greater for the MASE time period  
211 (mean of 4 km) than for the G-GAP time period (0.8 km). In fact, the longitude of G-GAP  
212 tremors is the most well-resolved parameter. As expected, the depth is the least well-resolved  
213 parameter. The westernmost and eastern tremor depths are poorly constrained for the MASE  
214 time period, which may explain the apparent depth trend in Figure 2 **c**.

215 To better resolve the spatial variations in the tremor locations, Figure 4 shows the number  
216 of tremors within each  $2 \times 2$  km square of the location region; note that  $1\sigma$  horizontal location  
217 errors are within this range (Figure 3 **a**, **b**, and **d**). The 50% tremor activity contour shows that  
218 during the MASE time period the sweet spot is composed of two high-density tremor zones in  
219 the strike direction, as for the G-GAP time period. The first zone, located next to the MASE  
220 stations, is close to the eastern cluster observed during the G-GAP time period, and is slightly  
221 elongate in the dip direction. The point with the highest number of tremors (in the eastern part of  
222 the cluster) is about 13 km west of the point with the highest number of tremors during the G-  
223 GAP time period, and less than 2 km from the 70% tremor activity contour of Figure 4 **b**. This is  
224 relatively close, compared with the 40 km separation of the two G-GAP clusters; consequently,  
225 we infer that these two patches are coincident. The second high-density tremor cluster during the  
226 MASE time period is elongate in the strike direction and located east of the second G-GAP  
227 cluster. This could be related to the previously observed errors in longitude (Figure 3 **c**); it is  
228 possible that this cluster is truly located farther west.

229 As previously shown by *Husker et al.* [2012], the spatiotemporal plot (Figure 2 **d**)  
230 indicates that tremors in the transient zone are active mainly during the SSEs, while the sweet  
231 spots are persistently active. Even with the G-GAP dataset, some activity is seen south of the  
232 sweet spots at the time of the SSE (Figure 2 **d**). This activity increases during the second phase  
233 of the 2009–2010 SSE, after the Maule earthquake (Figure 2 **e**). Some punctual tremor activity is  
234 also seen in the transient zone during the inter-SSE period. This tremor activity is consistent with  
235 the LFE activity used to detect short-term slow slip by *Frank et al.* [2015] and the timing of  
236 these tremor bursts correspond to the timing of the LFE bursts.

## 237 **5 Moment tensor estimation in the VLF band**

238 With the MASE dataset, 7 focal mechanisms can be estimated in the updip transient zone  
239 and 17 in the downdip cluster. Using the G-GAP data, 16 focal mechanisms can be estimated,  
240 comprising 9 and 7 solutions for the West and East clusters, respectively (Table S1 in the  
241 supporting information). The same numbers of focal mechanisms are estimated in the downdip  
242 clusters for the two time periods. Figure 5 shows an example of well-constrained solutions for  
243 both datasets. A total of 261 tremors are stacked for MASE solution and 1003 tremors for the G-  
244 GAP solution. The stacking results show well-identified signals on the vertical and horizontal  
245 channels. The gray curves, indicating solutions obtained from 1000 times bootstrap resampling  
246 of the data, suggest that the focal mechanism solutions are reliable. The focal mechanisms for the  
247 other points (Figure 6) are also consistent with shear slip on the plate interface. The variance  
248 reduction ranges from 20% to 77% for the G-GAP dataset, and 43% and 73% for MASE dataset,  
249 comparable to values obtained for VLF signals in Japan [*Ide and Yabe, 2014*]. The low minimum  
250 variance reduction for the G-GAP time period is probably due to the low number of available  
251 stations, which naturally reduces the signal-to-noise ratio, particularly when few tremors are  
252 available. The slip direction is similar between the two time periods, with only a few degrees of  
253 difference (N200°E and N204°E, respectively). These values are consistent with the plate  
254 convergence direction of N212°E.

255 No variations in focal mechanism orientations or depths are observed between clusters.  
256 On the other hand, some variations in fault plane orientation are observed between the two time  
257 periods. While the fault planes for the G-GAP time period are nearly horizontal, and thus  
258 consistent with the subduction interface geometry, some inclination is commonly seen in the  
259 MASE time period, with a normal oriented N290°E and a dip of 20–35° (Figure 6 **f**). This is  
260 similar to the observed trend in depths of tremor hypocenters. As the latter appears to be an  
261 artifact of network geometry, this fault plane inclination is probably also an artifact.

262 The average depth of these VLF events is a little deeper than the plate interface,  
263 estimated at about 43 km for this area [*Kim et al., 2010*]. However, considering depth as a  
264 function of variance reduction for a well-determined solution (Figure 5), we see uncertainty in  
265 our depth determination.

266 VLF magnitudes range from 2.2 to 2.6, and estimated durations,  $T$ , range from 14 to 20 s.  
267 These values are comparable with, or slightly smaller than, those estimated for VLF signals in  
268 western Japan [*Ide and Yabe, 2014*]. For G-GAP data, the magnitudes in the transient zone are  
269 slightly larger than the magnitudes of events in the sweet spots (Figure 7). This relationship is  
270 less clear for the MASE results in the sweet spot, but the events closer to the stations all have  
271 magnitudes of 2.4; i.e., the same magnitude as the colocated G-GAP events. This magnitude is  
272 also lower than 2.6; i.e., the magnitude of events within the transient zone. Events with the larger

273 magnitude located within the sweet spots are farther from the stations; hence, their solutions  
274 might be poorly constrained. These variations between clusters suggest that the size of VLF  
275 events varies along dip.

## 276 **6 Matched filter detection and characterization of additional VLF signals**

277 Our observations of simultaneous VLF signals and tremors do not necessarily imply that  
278 VLF signals are always accompanied by tremors. This is important because we suppose tremors  
279 and VLF earthquakes are different expressions of the same phenomena. While statistically this  
280 assumption seems justified it remains to be verified for individual events. To check whether VLF  
281 earthquakes can occur alone, we try to detect them independently of tremor bursts using a  
282 matched filtering algorithm.

283 We use the stacked VLF signal as a template for this procedure. Only vertical records are  
284 used, because the signal-to-noise ratio in the horizontal components (Figure 5) is not large  
285 enough to enable detection. For this approach, we reduce the number of MASE stations used to  
286 10 (Figure 1), because the computations are too time-consuming when using all MASE stations.  
287 Thus, during the MASE time period, these stacked template signals are cross-correlated against  
288 the seismograms of permanent SSN stations and 10 MASE stations. A network correlation  
289 coefficient (NCC) is then defined for location  $i$  at time  $j$ :

$$290 \quad NCC = \sum_s CC_s. \quad (4)$$

291 Where  $CC_s$  is the correlation coefficient at station  $s$ .

292 Only one set of templates (i.e., one point) is considered for each of the three clusters  
293 (each cluster in the downdip zone + the transient zone), because the network correlation  
294 coefficient shows little variation between consecutive points. The points considered are listed in  
295 Table S1 in the supporting information. Seismograms are scanned in 100s time windows with 1 s  
296 interval. If the NCC exceeds 8 for the first time period or 3.5 for the second time period, a  
297 detection is declared. These thresholds correspond to a mean value above 0.5 for each dataset. To  
298 avoid false positive detections from teleseismic earthquakes, detections are checked against the  
299 ANSS catalogue. This procedure detects 11 additional VLF earthquakes (Figure 8; Table S2 in  
300 the supporting information), with clear Z component signals. These new VLF events are  
301 consistent with the hypothesis that each VLF earthquake is accompanied by a tremor burst  
302 (Figure 8). We could not find any VLF event in the absence of tremor.

303 We now determine event focal mechanisms and evaluate locations in more detail. We  
304 only use vertical component data to determine the hypocenters and moment tensors of each  
305 event, which means that the problem is underdetermined. In addition, during the MASE time  
306 period we can see that the fault plane is not well resolved (Figure 6 f), presumably due to the  
307 network configuration. Consequently, for the isolated VLF events we only attempt to determine  
308 a slip direction and magnitude. We impose a dip of  $0^\circ$  or  $10^\circ$  (low-angle fault), a strike of  $-68^\circ$ ,  
309 and a slip direction between  $-130^\circ$  and  $-180^\circ$  (the main range of values obtained from VLF  
310 stacking). To determine the best location and focal mechanism, a grid search is performed to  
311 maximize the variance reduction. Every MASE station used in the stacking process is used for  
312 the moment tensor determination.

313 All focal mechanism solutions are low-angle thrusts, as expected from the constraints  
314 imposed. The mechanisms themselves are similar, but their slip directions vary a little between  
315 clusters, with a mean value of N195°E for the transient zone, N203°E for the western sweet spot,



316 and N230°E for the eastern sweet spot. Event depths vary from 30 km to 54 km, suggesting that  
317 this parameter is poorly constrained, even if the variance reduction is relatively high. Their  
318 magnitudes are between 3.0 and 3.4, which are similar to observations of VLF signals in Japan  
319 [Ito *et al.*, 2007], but nearly one unit of magnitude larger than the typical size of VLF events  
320 estimated from waveform stacking (mean  $M_w$  of 3.2, compared with 2.4). Moreover, the  
321 magnitudes of the events located in the transient zone are lower than those of the events within  
322 the sweet spot, which is the opposite of the relationship suggested by the stacked waveforms.

## 323 **7 Discussion**

324 Comparing the MASE and G-GAP datasets allows us to obtain a better picture of how  
325 tremor locations in Guerrero relate to tectonics and the source process. The results obtained from  
326 the MASE dataset, while consistent with previous studies that used the same data [Payero *et al.*,  
327 2008; Husker *et al.*, 2012; Frank *et al.*, 2014; Cruz-Atienza *et al.*, 2015], only provide greater  
328 resolution along dip. The most recent G-GAP dataset reveals that the tremor activity in Guerrero  
329 is patchier than previously thought. Careful analysis of the MASE dataset seems to confirm this  
330 patchy tremor location. Although we have already proposed that different network geometries  
331 are probably responsible for the different tremor distributions, there are also differences in the  
332 seismic phase types used for each network. We have assumed that tremor is composed mostly of  
333 S waves, but tremor during the G-GAP time period is detected using principally vertical  
334 components of seismograms, which includes a significant contribution of P waves.

335 To evaluate the impact of restricting locations to vertical component data, tremor  
336 locations are also computed during the MASE time period using the permanent SSN network  
337 with vertical component data from the temporary network. Five times less tremors are detected  
338 in the absence of horizontal component data. Tremor locations are also slightly different (Figure  
339 9). While the differences in latitude are small ( $0.1 \pm 5.0$  km), the differences in longitude and  
340 depth are as large as  $0.8 \pm 18.0$  km and  $3 \pm 11$  km, respectively. These larger errors in longitude are  
341 probably due to the linear configuration of the network, since the latitude is well-determined; we  
342 anticipate that poorly resolved longitudes should not be a problem for the G-GAP time period.  
343 Despite the reduced detectability and poorly constrained depths, analysis with only vertical  
344 sensors produces similar results.

345 To confirm the patchy tremor distribution, we compare our results with the tremor  
346 locations obtained with the TREP method [Cruz-Atienza *et al.*, 2015]. Since TREP explains the  
347 energy spatial distribution and the particle motion polarization azimuth of tremor signals,  
348 locations with this method are independent of those yielded by our envelope correlation  
349 technique. Because we are interested in the horizontal segmentation of tremors, we constrained  
350 the TREP search range to between 40 and 50 km depth. More than 78,000 locations with  
351 resolution lengths smaller than 10 km are determined, and display three main source clusters  
352 (Figure 10), with the southernmost one lying in the transient zone. Locations in the sweet spot  
353 are also segmented into two clusters along the trench-parallel direction, with some activity  
354 between them (one order of magnitude lower). Although the maxima of the clusters found with  
355 TREP are shifted 10 km SE and 34 km SSW of the corresponding values for envelope  
356 correlation, the overall comparison is consistent (i.e., contours of 70% tremor activity  
357 significantly overlap in both cases; see gray contours in Figure 10). We therefore conclude that  
358 tremor activity during the G-GAP period was segmented in at least two clusters separated by ~40  
359 km from each other in the trench-parallel direction.

360 While the width of the tremor zone is considerably larger in Guerrero, the patchy  
361 distribution of tremors is similar to tremor distribution in Jalisco, in the northern part of the  
362 Mexican subduction zone [Ide, 2012]. In the southern part of the subduction zone, tremors have  
363 been detected in Oaxaca [Brudzinski et al., 2010]. They are also located around 40 km downdip  
364 of the SSEs, but with a less patchy distribution than in Jalisco. SSEs in Mexico nucleate either in  
365 Guerrero or Oaxaca, but they have been observed bridging the gap between the two areas  
366 [Graham et al., 2015]. This means that slow deformation is occurring between the two tremor  
367 regions, and that tremors could also be observed between these areas. It may only be due to the  
368 lack of seismic stations that we have not yet found tremor patches in other parts of the Mexican  
369 subduction zone (Figure 1). More investigation is needed along the 40 km iso-depth contour to  
370 confirm this hypothesis.

371 The along-strike segmentation of tremor activity may reveal small-scale variations in the  
372 geometry of the plate interface (i.e., subducted irregularities) and/or in the mechanical properties  
373 of the fault zone close to the interface (e.g., gradients in permeability and thus in pore pressure).  
374 Temporal changes of the permeability have been proposed to reconcile observations that suggest  
375 both transient and heterogeneous fluid content along the Barbados margin decollement [Saffer  
376 and Tobin, 2011]. There is also geological evidence [Fagereng, 2011; Collettini et al., 2011]  
377 suggesting that subducted heterogeneities are linked to the slow slip phenomena. Numerical  
378 modeling studies [Ando et al., 2010; Skarbek et al., 2012] show that heterogeneities in the  
379 frictional properties of the plate interface lead to tremor like behaviors of the dislocation process.  
380 The distribution of the heterogeneities would then control the tremor distribution. The diversity  
381 of tremor distributions along the Mexican subduction zone from very patchy to nearly  
382 continuous would be due to variations in density of the heterogeneities.

383 A clear increase in tremor detections is seen during the 2006 SSE (Figure 2 **d**), not only  
384 in the transient zone but also in the sweet spots as was also seen with LFE activity [Frank et al.,  
385 2015]. This is less clear for the 2009–2010 SSE. Some tremor activity is observed south of the  
386 sweet spots during this SSE, which is probably related to the tremor in the transient zone. This  
387 activity is limited to the 2009–2010 SSE time period, confirming the transient nature of tremor in  
388 the updip patch. However, no clear increase in tremor detection is observed in the sweet spots, as  
389 for the 2006 SSE. This result may be due to the stations being not yet fully in service during the  
390 SSE, but it may also indicate that the sweet spots were not fully activated by the time of this  
391 SSE. This could be because the stress perturbation following the Maule earthquake that triggered  
392 tremors in the sweet spot, [Zigone et al., 2012] activated a short-term slow slip [Frank et al.,  
393 2015] and already discharged the sweet spot. An analysis of the time evolution of tremor  
394 detections with GPS displacements is needed to confirm this observation.

395 Some of the focal mechanisms of the VLF events obtained during the MASE time period  
396 suggest a variation in the slope of the subduction zone interface, dipping to the west; however,  
397 this is not confirmed by the G-GAP results. Considering the uncertainty on the EW location of  
398 tremors from the MASE dataset, we suspect that this western dip angle is an artifact. In fact,  
399 when we move the source location to the east, the dip angle increases to the west (Figure 11),  
400 although the variance reductions of the solutions are similar. In conclusion, the fault planes  
401 obtained with MASE data are not well constrained, even if the observations are well explained  
402 (variance reduction of 73%); only the slip direction seems to be robust. The mechanisms with  
403 variations in their fault plane directions coincide with the deeper located tremors and with the

404 area where the second concentration of tremors occurs. This suggests that these events are in fact  
405 located farther westward, which coincides with the western cluster of the G-GAP time period.

406 Analysis of VLF earthquakes in other regions [Ito *et al.*, 2007] indicates that these  
407 earthquakes occur as shear slip on the subduction interface. Our results seem coherent with this  
408 interpretation, but the depth of the VLF events in this study is slightly greater than the  
409 subduction interface and greater than the depths of the LFEs [Frank *et al.*, 2014]. Several  
410 structural studies have been undertaken of the Mexican subduction interface [Pardo and Suarez,  
411 1995; Pérez-Campos *et al.*, 2008; Kim *et al.*, 2010] and they are generally in agreement with the  
412 flat and almost horizontal segment of the interface in Guerrero. However, the depth of this flat  
413 segment varies by a few kilometers depending on the model, and our depth estimation has  
414 significant uncertainty. Therefore, we cannot definitively conclude whether VLF events occur on  
415 the interface or deeper.

416 VLF magnitudes obtained from waveform stacking vary along the plate interface, with a  
417 higher magnitude updip. This is not confirmed by the magnitudes of the independent VLF  
418 earthquakes estimates. Since the depths of these events are also highly variable, and there is a  
419 trade-off between depth and magnitude, this implies that the magnitude is also poorly  
420 constrained. Moreover, the moment tensor estimates obtained from the stacked waveform data  
421 give a mean estimate, and some occasional events can be of lower magnitude. The differences in  
422 magnitudes between the moment tensors of stacked and isolated events (mean  $M_w$  of about 2.4,  
423 compared with 3.2) probably reflect the isolated VLF events being the largest events, although  
424 we cannot exclude the possibility that stacked events are affected by waveform misalignment. In  
425 addition, the sample of individual events is very small (only two events in the transient zone) so  
426 more observations are needed to conclude one way or another on this variation of magnitude.

427 From analysis of LFEs, mainly before the 2006 SSE, Frank *et al.* [2013] identified a low-  
428 angle thrust fault consistent with our observations. They found a slip direction rotated slightly  
429 clockwise from the convergence direction; in contrast, our results are rotated anti-clockwise by  
430 8–12°. Cruz-Atienza *et al.* [2015] suggested a slip direction sub-parallel to the convergence  
431 direction. Both results are generally consistent with ours. However, we find a slip direction  
432 closer to the dip direction than to the convergence direction (Figure 6), even if there is only 10°  
433 difference between the two directions. Radiguet *et al.* [2012] found that a slip direction sub-  
434 parallel to the dip direction was more appropriate for the 2006 SSE, in agreement with our  
435 results, whereas a slip direction sub-parallel to the convergence direction better explained the  
436 2009–2010 SSE. Further investigation is needed to corroborate the slip directions of the SSEs; if  
437 such a difference is verified, then a component of left-lateral strike-slip movement would be  
438 needed to accommodate the stress field.

439 The data of the two time periods have been fully scanned, but we only find VLF signals  
440 during tremors bursts. This suggests that VLF earthquakes do not occur in the absence of  
441 tremors. The same suggestion has been made for Japan [Ito *et al.*, 2007; Takeo *et al.*, 2010]. Due  
442 to the high levels of noise in the VLF band, however, our VLF catalog is not complete for this  
443 region. Thus, it is still possible that undetected, isolated VLF earthquakes occurred.

## 444 **8 Conclusions**

445 The envelope correlation method was used to study non-volcanic tremors recorded by  
446 two different experiments in Guerrero, Mexico. Results show significant variability in tremor

447 locations, depending on the dataset. This underlines the importance of adequate network  
448 configuration for location techniques. Locations of the more recent G-GAP dataset, which had  
449 better spatial coverage, reveal that tremor activity in the sweet spot is segmented into two  
450 clusters separated by 40 km in the trench-parallel direction. This finding indicates that tremor  
451 sources are patchier than previously thought, and that other tremor clusters may exist, and could  
452 be found in Mexico if denser seismic networks were installed. This probably reflects small-scale  
453 variations in the interface geometry and/or heterogeneities in fluid content within the fault zone.

454 Moment tensor solutions obtained from stacked VLF waveforms show focal mechanisms  
455 with slip directions close to the plate dip direction. If correct, this means that some left-lateral  
456 strike-slip deformation is being accommodated in the continental plate. The best-resolved focal  
457 mechanisms are consistent with a sub-horizontal fault plane with depths close to the depth of the  
458 subduction interface. The magnitudes of these events are generally higher in the transient zone  
459 than for the sweet spot clusters. This variation is similar to that observed in other subduction  
460 zones.

461 Routine and independent detection of VLF earthquakes only reveals events during tremor  
462 activity. This suggests that VLF events only occur during tremor bursts, similar to the LFEs or  
463 tremors that are concomitant with SSE [Frank *et al.*, 2014; Zigone *et al.*, 2012]. This may,  
464 however, be due to catalogue incompleteness.

## 465 **9 Acknowledgments and Data**

466 We thank all the volunteers who made the operation of the MASE and G-GAP arrays  
467 possible and for the data used in this study  
468 ([http://www.gps.caltech.edu/~clay/MASEdir/data\\_avail.html](http://www.gps.caltech.edu/~clay/MASEdir/data_avail.html), G-GAP data are available upon  
469 request at IsTerre). SSN data were obtained by the Servicio Sismológico Nacional (México),  
470 whose staff are acknowledged for station maintenance, data acquisition, and data distribution.  
471 The G-GAP experiment was funded by the Agence Nationale de la Recherche (France) under  
472 contract RA0000CO69 (ANR G-GAP). GMT software [Wessel and Smith, 1991] was used to  
473 generate the figures.

474 We thank the Associate Editor and an anonymous reviewer for their helpful comments.

## 475 **10 References**

- 476 Ando, R., R. Nakata, and T. Hori (2010), A slip pulse model with fault heterogeneity for low-  
477 frequency earthquakes and tremor along plate interfaces, *Geophys. Res. Lett.*, 37,  
478 L10310, doi:10.1029/2010GL043056.
- 479 Ando, M., Y. Tu, H. Kumagai, Y. Yamanaka, and C.-H. Lin (2012), Very low frequency  
480 earthquakes along the Ryukyu subduction zone, *Geophys. Res. Lett.*, 39, L04303,  
481 doi:10.1029/2011GL050559.
- 482 Beroza, G., and S. Ide (2011). Slow earthquakes and nonvolcanic tremor, *Annu. Rev. Earth  
483 Planet. Sci.*, 39, 271-296, doi:10.1146/annurev-earth-040809-152531.
- 484 Brown, J.R., G.C. Beroza, and D.R. Shelly (2008), An autocorrelation method to detect low  
485 frequency earthquakes within tremor, *Geophys. Res. Lett.*, 35, L16305,  
486 doi:10.1029/2008GL034560.

- 487 Brown, J.R., G.C. Beroza, S. Ide, K. Ohta, D.R. Shelly, S.Y. Schwartz, W. Rabbel, M. Thorwart,  
488 and H. Kao (2009), Deep low-frequency earthquakes in tremor localize to the plate  
489 interface in multiple subduction zones, *Geophys. Res. Lett.*, 36, L19306,  
490 doi:10.1029/2009GL040027.
- 491 Brudzinski, M.R., and R.M. Allen (2007), Segmentation in episodic tremor and slip along  
492 Cascadia, *Geology*, 35(10), 907-910, doi:10.1130/G23740A.1.
- 493 Brudzinski, M.R., H.R. Hinojosa-Prieto, K.M. Schlanser, E. Cabral-Cano, A. Arciniega-  
494 Ceballos, O. Diaz-Molina, and C. Demets (2010), Nonvolcanic tremor along the Oaxaca  
495 segment of the Middle America subduction zone, *J. Geophys. Res.*, 115, B00A23, doi:  
496 10.1029/2008JB006061.
- 497 Collettini, C., A. Niemeijer, C. Viti, S.A.F. Smith, and C. Marone (2011), Fault structure,  
498 frictional properties and mixed-mode fault slip behavior. *EPSL*, 311, 316-327, doi:  
499 10.1016/j.epsl.2011.09.020.
- 500 Cruz-Atienza, V.M., A. Husker, D. Legrand, E. Caballero, and V. Kostoglodov (2015),  
501 Nonvolcanic tremor locations and mechanisms in Guerrero, Mexico, from energy-based  
502 and particle motion polarization analysis, *J. Geophys. Res.*, 120(1), 275-289,  
503 doi:10.1002/2014JB011389.
- 504 Fagereng, A. (2011), Frequency-size distribution of competent lenses in a block-in-matrix  
505 mélange: imposed length scales of brittle deformation?, *J. Geophys. Res.*, 116, B05302,  
506 doi: 10.1029/2010JB007775.
- 507 Frank, W.B., N.M. Shapiro, V. Kostoglodov, A.L. Husker, M. Campillo, J.S. Payero, and G.A.  
508 Prieto (2013), Low-frequency earthquakes in the Mexican sweet spot, *Geophys. Res.*  
509 *Lett.*, 40, 2661-2666, doi:10.1002/grl.50561.
- 510 Frank, W.B., N.M. Shapiro, A.L. Husker, V. Kostoglodov, A. Romanenko, and M. Campillo  
511 (2014), Using systematically characterized low-frequency earthquakes as a fault probe in  
512 Guerrero, Mexico, *J. Geophys. Res.*, 119, doi:10.1002/2014JB011457.
- 513 Frank, W.B., M. Radiguet, B. Rousset, N.M. Shapiro, A.L. Husker, V. Kostoglodov, N. Cotte,  
514 and M. Campillo (2015), Uncovering the geodetic signature of silent slip through  
515 repeating earthquakes, *Geophys. Res. Lett.*, 42, 2774-2779, doi:10.1002/2015GL063685.
- 516 Ghosh, A., J.E. Vidale, J.R. Sweet, K.C. Kreager, and A.G. Wech (2009), Tremor patches in  
517 Cascadia revealed by seismic array analysis, *Geophys. Res. Lett.*, 36, L17316,  
518 doi:10.1029/2009GL039080.
- 519 Graham, S., C. DeMets, E. Cabral-Cano, V. Kostoglodov, B. Rousset, A. Walpersdorf, N. Cotte,  
520 C. Lasserre, R. McCaffrey, and L. Salazar-Tlaczani (2015), Slow slip history for the  
521 Mexico subduction zone: 2005 through 2011. *Pure Appl. Geophys.*, doi: 10.1007/s00024-  
522 015-1211-x.
- 523 Husker, A., S. Peyrat, N. Shapiro, and V. Kostoglodov (2010), Automatic non-volcanic tremor  
524 detection in the Mexican subduction zone, *Geofis. Int.*, 49(1), 17-25.
- 525 Husker, A.L., V. Kostoglodov, V.M. Cruz-Atienza, and D. Legrand (2012), Temporal variations  
526 of non-volcanic tremor (NVT) locations in the Mexican subduction zone: finding the  
527 NVT sweet spot, *Geochem. Geophys. Geosyst.*, 13(3), doi:10.1029/2011GC003916.

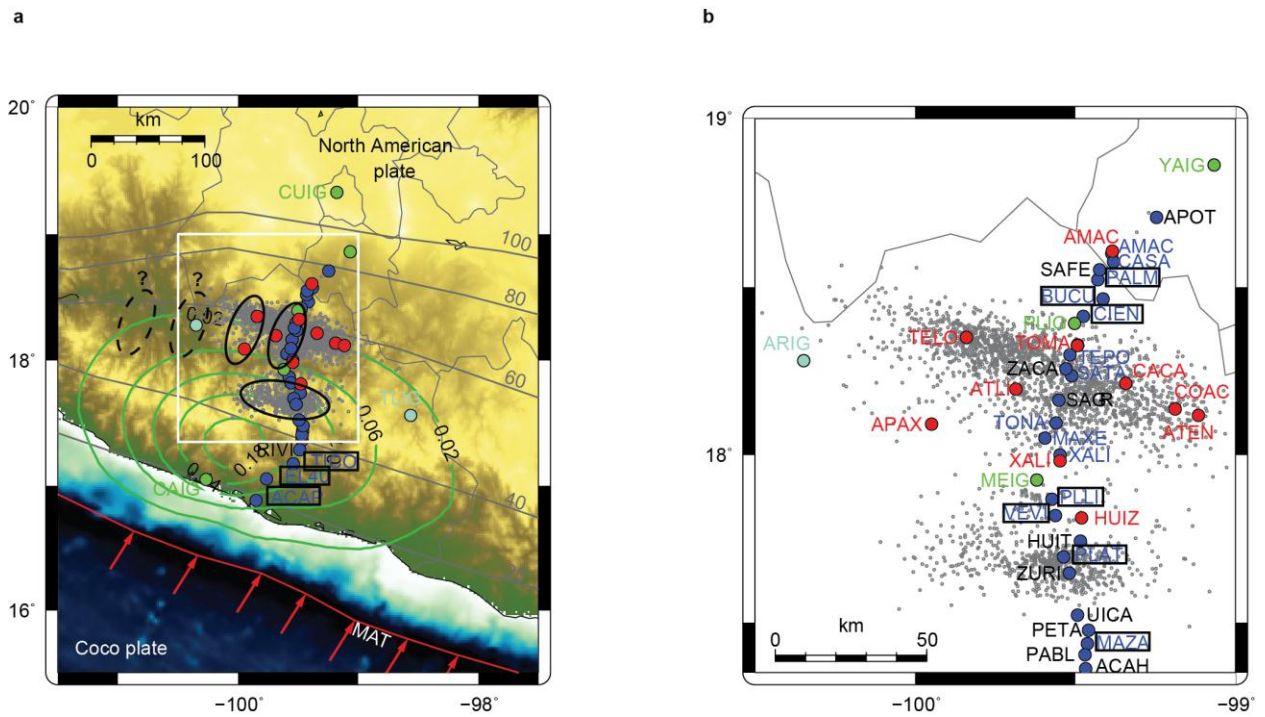
- 528 Ide, S., (2010), Striations, duration, migration and tidal response in deep tremor, *Nature*, 466,  
529 356-359, doi:10.1038/nature09251.
- 530 Ide, S., (2012), Variety and spatial heterogeneity of tectonic tremor worldwide, *J. Geophys. Res.*,  
531 117, B03302, doi:10.1029/2011JB008840.
- 532 Ide, S., and S. Yabe (2014), Universality of slow earthquakes in the very low frequency band,  
533 *Geophys. Res. Lett.*, 41, 2786-2793, doi:10.1002/2014GL059712.
- 534 Ide, S., G.C. Beroza, D.R. Shelly, and T. Uchide (2007a), A scaling law for slow earthquakes,  
535 *Nature*, 447, doi:10.1038/nature05780.
- 536 Ide, S., D.R. Shelly, and G.C. Beroza (2007b), Mechanism of deep low frequency earthquakes:  
537 Further evidence that deep non-volcanic tremor is generated by shear slip on the plate  
538 interface, *Geophys. Res. Lett.*, 34, L03308, doi:10.1029/2006GL028890.
- 539 Ide, S., S. Yabe, H.-J. Tai, and K.H. Chen (2015), Thrust-type focal mechanisms of tectonic  
540 tremors in Taiwan: Evidence of subduction, *Geophys. Res. Lett.*, 42, 3248-3256,  
541 doi:10.1002/2015GL063794.
- 542 Iglesias, A., S.K. Singh, A.R. Lowry, M. Santoyo, V. Kostoglodov, K.M. Larson, and I. Franco-  
543 Sánchez (2004), The silent earthquake of 2002 in the Guerrero seismic gap, Mexico  
544 (Mw=7.6): Inversion of slip on the plate interface and some implications, *Geofísica*  
545 *Internacional*, 43(3), 309-317.
- 546 Iglesias, A., R.W. Clayton, X. Pérez-Campos, S.K. Singh, J.F. Pacheco, D. García, and C.  
547 Valdés-González (2010), S wave velocity structure below central Mexico using high-  
548 resolution surface wave tomography, *J. Geophys. Res.*, 115, B06307,  
549 doi:10.1029/2009JB006332.
- 550 Imanishi, K., T. Uchide, and N. Takeda (2016), Determination of focal mechanisms of  
551 nonvolcanic tremor using S wave polarization data corrected for the effects of anisotropy,  
552 *Geophys. Res. Lett.*, 43, 611-619, doi:10.1002/2015GL067249.
- 553 Ito, Y., K. Obara, K. Shiomi, S. Sekine, and H. Hirose (2007), Slow earthquakes coincident with  
554 episodic tremors and slow slip events, *Science*, 315, 503-506,  
555 doi:10.1126/science.1134454.
- 556 Ito, Y., K. Obara, T. Matsuzawa, and T. Maeda (2009), Very low frequency earthquakes related  
557 to small asperities on the plate boundary interface at the locked to aseismic transition, *J.*  
558 *Geophys. Res.*, 114, B00A13, doi:10.1029/2008JB006036.
- 559 Kao, H., S.-J. Shan, H. Dragert, G. Rogers, J.F. Cassidy, and K. Ramachandran (2005), A wide  
560 depth distribution of seismic tremors along the northern Cascadia margin, *Nature*, 436,  
561 841-844, doi:10.1038/nature03903.
- 562 Kennett, B.L.N., E.R. Engdahl, and R. Buland (1995), Constraints on seismic velocities in the  
563 Earth from travel times, *Geophys. J. Int.*, 122, 108-124.
- 564 Kim, Y., R.W. Clayton, and J.M. Jackson (2010), Geometry and seismic properties of the  
565 subducting Cocos plate in central Mexico, *J. Geophys. Res.*, 115, B06310,  
566 doi:10.1029/2009JB006942.

- 567 Kostoglodov, V., S. K. Singh, J. A. Santiago, S. I. Franco, K. M. Larson, A. R. Lowry, and R.  
568 Bilham (2003), A large silent earthquake in the Guerrero seismic gap, Mexico, *Geophys*  
569 *Res Lett*, 30(15), doi:10.1029/2003GL017219.
- 570 Kostoglodov, V., A. Husker, N.M. Shapiro, J.S. Payero, M. Campillo, N. Cotte, and R. Clayton  
571 (2010), The 2006 slow slip event and nonvolcanic tremor in the Mexican subduction  
572 zone, *Geophys. Res. Lett.*, 37, L24301, doi:10.1029/2010GL045424.
- 573 La Rocca, M., K.C. Creager, D. Galluzzo, S. Malone, J.E. Vidale, J.R. Sweet, and A.G. Wech  
574 (2009), Cascadia tremor located near plate interface constrained by S minus P wave  
575 times, *Science*, 323, 620-623, doi:10.1126/science.1167112.
- 576 Larson, K. M., V. Kostoglodov, S. Miyazaki, and J. A. S. Santiago (2007), The 2006 aseismic  
577 slow slip event in Guerrero, Mexico: New results from GPS, *Geophys Res Lett*, 34,  
578 L13309, doi 10.1029/2007GL029912.
- 579 MASE (2007), Meso-America Subduction Experiment (MASE) data set,  
580 doi:10.7909/C3RN35SP.
- 581 Nadeau, R.M., and D. Dolenc (2005), Nonvolcanic tremors deep beneath the San Andreas Fault,  
582 *Science*, 307, 389-389, doi:10.1126/science.1107142.
- 583 Obara, K., (2002), Nonvolcanic deep tremor associated with subduction in Southwest Japan,  
584 *Science*, 296, 1679-1681, doi:10.1126:science.1070378.
- 585 Obara, K., H. Hirose, F. Yamamizu, and K. Kasahara (2004), Episodic slow slip events  
586 accompanied by non-volcanic tremors in southwest Japan subduction zone. *Geophys.*  
587 *Res. Lett.*, 31(23), doi:10.1029/2004GL020848.
- 588 Outerbridge, K.C., T.H. Dixon, S.Y. Schwartz, J.I. Walter, M. Protti, V. Gonzalez, J. Biggs, M.  
589 Thorwart, and W. Rabbel (2010), A tremor and slip event on the Cocos-Caribbean  
590 subduction zone as measured by a global positioning system (GPS) and seismic network  
591 on the Nicoya Peninsula, Costa Rica, *J. Geophys. Res.*, 115, B10408,  
592 doi:10.1029/2009/JB006845.
- 593 Pardo, M., and G. Suarez (1995), Shape of the subducted Rivera and Coco plates in southern  
594 Mexico: seismic and tectonic implications, *J. Geophys. Res.*, 100(B7), 12,357-12,373,  
595 doi:10.1007/s004100050129.
- 596 Payero, J. S., V. Kostoglodov, N. Shapiro, T. Mikumo, A. Iglesias, X. Pérez-Campos, and R. W.  
597 Clayton (2008), Nonvolcanic tremor observed in the Mexican subduction zone, *Geophys.*  
598 *Res. Lett.*, 35, L07305, doi:10.1029/2007GL032877.
- 599 Peng, Z., and K. Chao (2008), Non-volcanic tremor beneath the Central Range in Taiwan  
600 triggered by the 2001 Mw 7.8 Kunlun earthquake, *Geophys. J. Int.*, 175, 825-829,  
601 doi:10.1111/j.1365-246X.2008.03886.x.
- 602 Peng, Z., and J. Gomberg (2010), An integrated perspective of the continuum between  
603 earthquakes and slow-slip phenomena, 3, 599-607, doi:10.1038/NGEO940.
- 604 Pérez-Campos, X., Y. Kim, A. Husker, P.M. Davis, R.W. Clayton, A. Iglesias, J.F. Pacheco,  
605 S.K. Singh, V.C. Manea, and M. Gurnis (2008), Horizontal subduction and truncation of  
606 the Cocos plate beneath central Mexico, *Geophys. Res. Lett.*, 35, L18303,  
607 doi:10.1029/2008GL0351127.

- 608 Radiguet, M., F. Cotton, M. Vergnolle, M. Campillo, B. Valette, V. Kostoglodov, and N. Cotte  
609 (2011), Spatial and temporal evolution of a long term slow slip event: the 2006 Guerrero  
610 slow slip event, *Geophys. J. Int.*, 184, 816-828, doi:10.1111/j.1365-246X.2010.04866.x.
- 611 Radiguet, M., F. Cotton, M. Vergnolle, M. Campillo, A. Walpersdorf, N. Cotte, and V.  
612 Kostoglodov (2012), Slow slip events and strain accumulation in the Guerrero gap,  
613 Mexico, *J. Geophys. Res.*, 117, doi:10.1029/2011JB008801.
- 614 Rogers, G., and H. Dragert (2003), Episodic tremor and slip on the Cascadia subduction zone:  
615 the chatter of silent slip, *Science*, 300, 1942-1943, doi:10.1126/science.1084783.
- 616 Royer, A. A., and M. G. Bostock (2014), A comparative study of low frequency earthquake  
617 templates in northern Cascadia, *Earth Pl. Sc. Lett.*, 402, 247-256.
- 618 Saffer, D.M., and H.J. Tobin (2011), Hydrogeology and mechanics of subduction zone forearcs:  
619 fluid flow and pore pressure, *An. Rev. Earth Planet. Sc.*, 39, 157-186,  
620 doi:10.1146/annurev-earth-040610-133408.
- 621 Schwartz, S.Y., and J.M. Rokosky (2007), Slow slip events and seismic tremor at circum-pacific  
622 subduction zones, *Rev. Geophys.*, 45, RG3004, doi:10.1029/2006RG000208.
- 623 Shelly, D.R., G.C. Beroza, S. Ide, and S. Nakamura (2006), Low-frequency earthquakes in  
624 Shikoku, Japan, and their relationship to episodic tremor and slip, *Nature*, 442, 188-191,  
625 doi:10.1038/nature04931.
- 626 Shelly, D.R., G.C. Beroza, and S. Ide (2007), Non-volcanic tremor and low-frequency  
627 earthquake swarms, *Nature*, 446, 305-307, doi:10.1038/nature05666.
- 628 Skarbek, R.M., A.W. Rempel, and D.A. Schmidt (2012), Geologic heterogeneity can produce  
629 aseismic slip transients. *Geophys. Res. Lett.*, 39, L21306, doi:10.1029/2012GL053762.
- 630 Takeo, A., K. Idehara, R. Iritani, T. Tonegawa, Y. Nagaoka, K. Nishida, H. Kawakatsu, S.  
631 Tanaka, K. Miyakawa, T. Iidaka, M. Obayashi, H. Tsuruoka, K. Shiomi, and K. Obara  
632 (2010), Very broadband analysis of a swarm of very low frequency earthquakes and  
633 tremors beneath Kii Peninsula, SW Japan, *Geophys. Res. Lett.*, 37, L06311,  
634 doi:10.1029/2010GL042586.
- 635 Wech, A.G., and K.C. Creager (2007), Cascadia tremor polarization evidence for plate interface  
636 slip, *Geophys. Res. Lett.*, 34, doi:10.1029/2007GL031167.
- 637 Wessel, P., and W.H. Smith (1991), Free software helps map and display data, *Eos Trans. AGU*,  
638 72(41), 441-446, doi: 10.1029/90EO00319.
- 639 Zigone, D., D. Rivet, M. Radiguet, M. Campillo, C. Voisin, N. Cotte, A. Walpersdorf, N.  
640 Shapiro, G. Cougoulat, P. Roux, V. Kostoglodov, A. Husker, and J.S. Payero (2012),  
641 Triggering of tremors and slow slip events in Guerrero, Mexico, by the 2010 Mw8.8  
642 Maule, Chile, earthquake, *J. Geophys. Res.*, 117, doi:10.1029/2012JB009160.



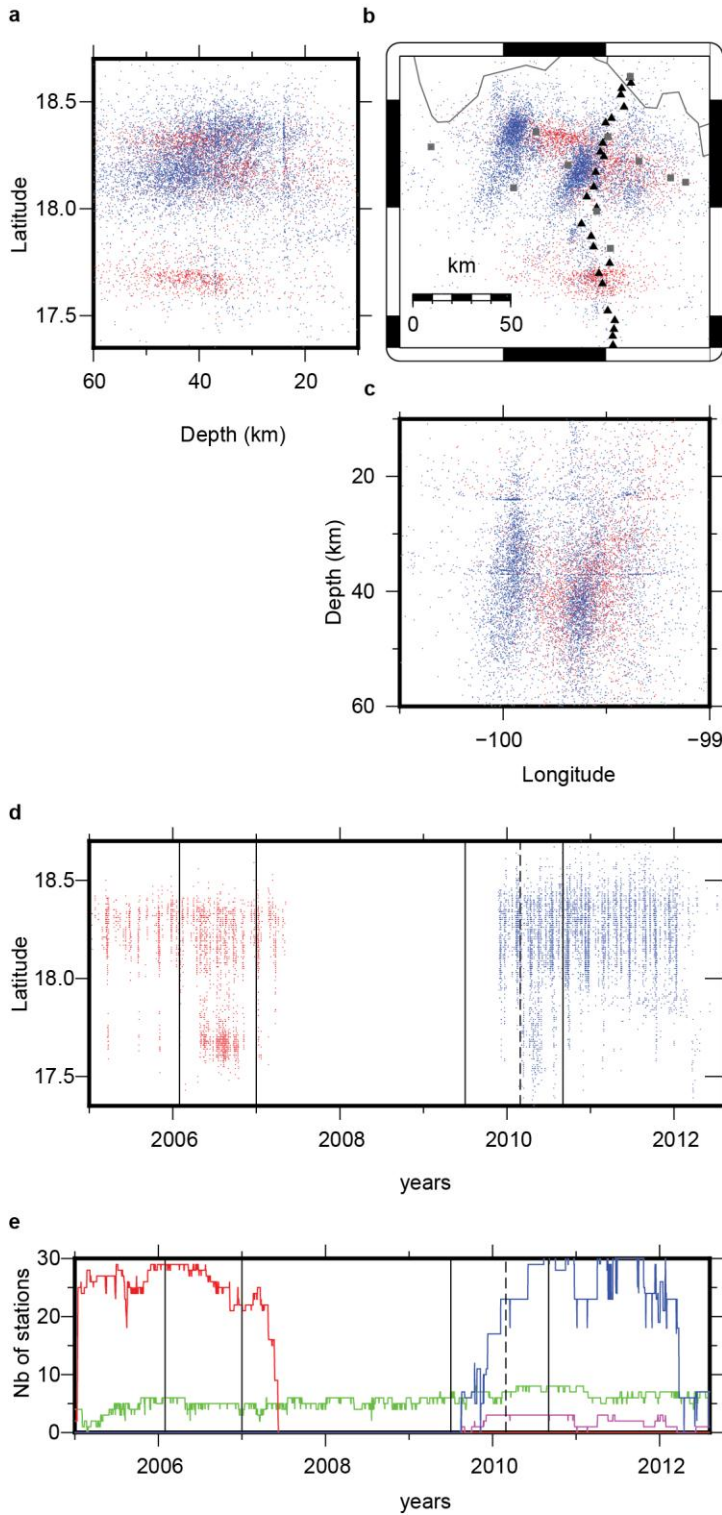
643 **Figures**



644

645 **Figure 1.** Study area in Guerrero, Mexico, showing station distributions for each experiment. **a**  
 646 Seismotectonic map. Grey circles indicate tremors located with the MASE array. The slip  
 647 distribution of the 2006 SSE is shown in green isocontours with 0.04 m spacing [Radiguet *et al.*,  
 648 2011]. Tremor clusters found in this study are indicated by black ellipses. Other potential clusters  
 649 are indicated by dashed black ellipses. Red arrows show the direction of convergence. Isodepth  
 650 contours of the subduction zone interface are indicated by grey lines [Pardo *et al.*, 1995]. **b**  
 651 Enlargement of the area outlined by the white rectangle in **a**. MASE stations are plotted as blue  
 652 circles; G-GAP stations are shown as red circles. Green circles are permanent SSN stations  
 653 installed before the MASE experiment; permanent stations installed after the MASE experiment

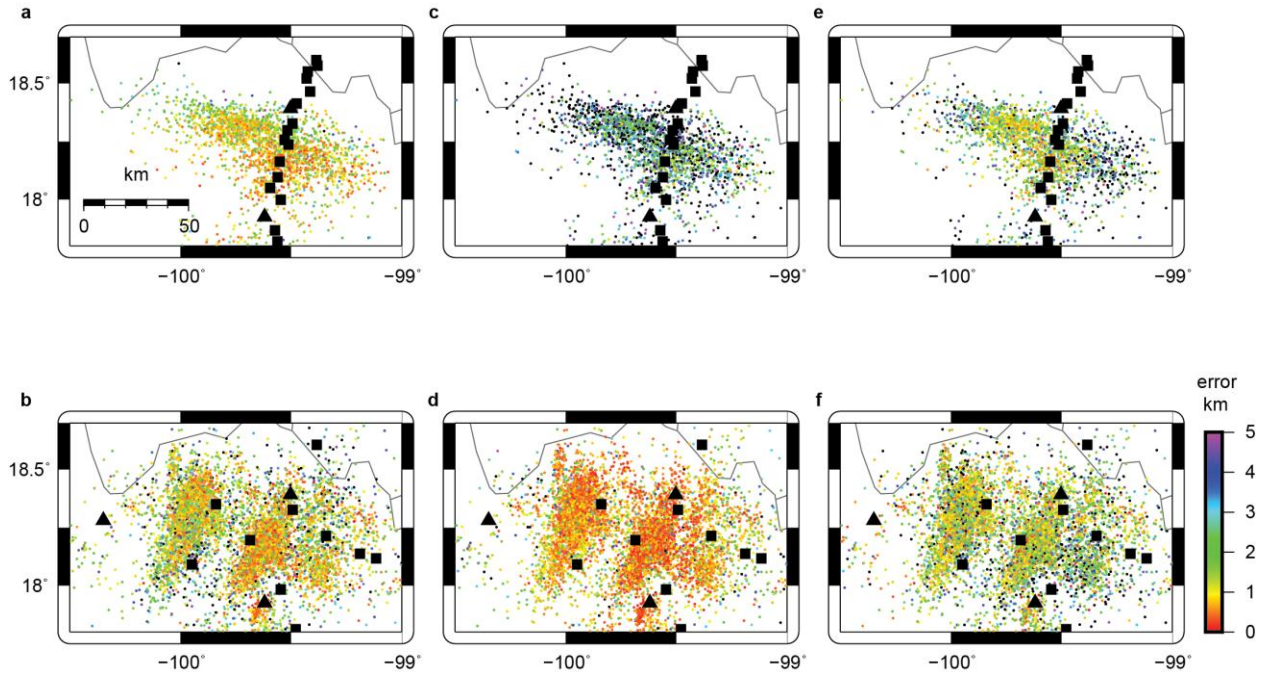
654 are indicated by cyan circles. MASE station names in blue are used for VLF stacking. MASE  
 655 station names framed by black rectangles are used to search for isolated VLF events.



656

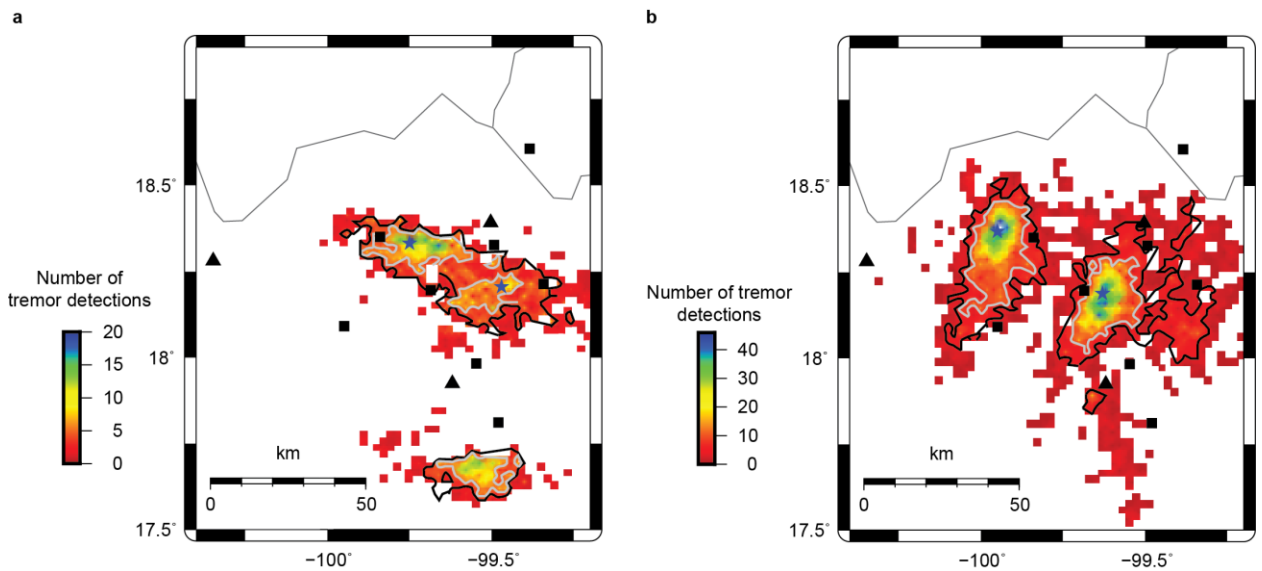
657 **Figure 2.** Tremor distribution. Tremors detected during the MASE time period are plotted in  
 658 blue, while those detected during the G-GAP time period are plotted in red. **a.** Tremor centroids

659 projected onto a north–south cross-section. **b.** Plane view of the tremor distribution. **c.** East–West  
 660 cross-section. **d.** Space–time plot of tremors. The black lines indicate the beginning and end of  
 661 the 2006 and 2009–2010 SSEs. The dashed line shows the time of occurrence of the February 27,  
 662 2010  $M_w$ 8.8 Maule earthquake. **e.** Station availability as a function of time. The MASE stations  
 663 are indicated in red, the G-GAP vertical short-period and three-component stations are indicated  
 664 in blue and magenta, respectively, and the permanent stations are indicated in green.



665

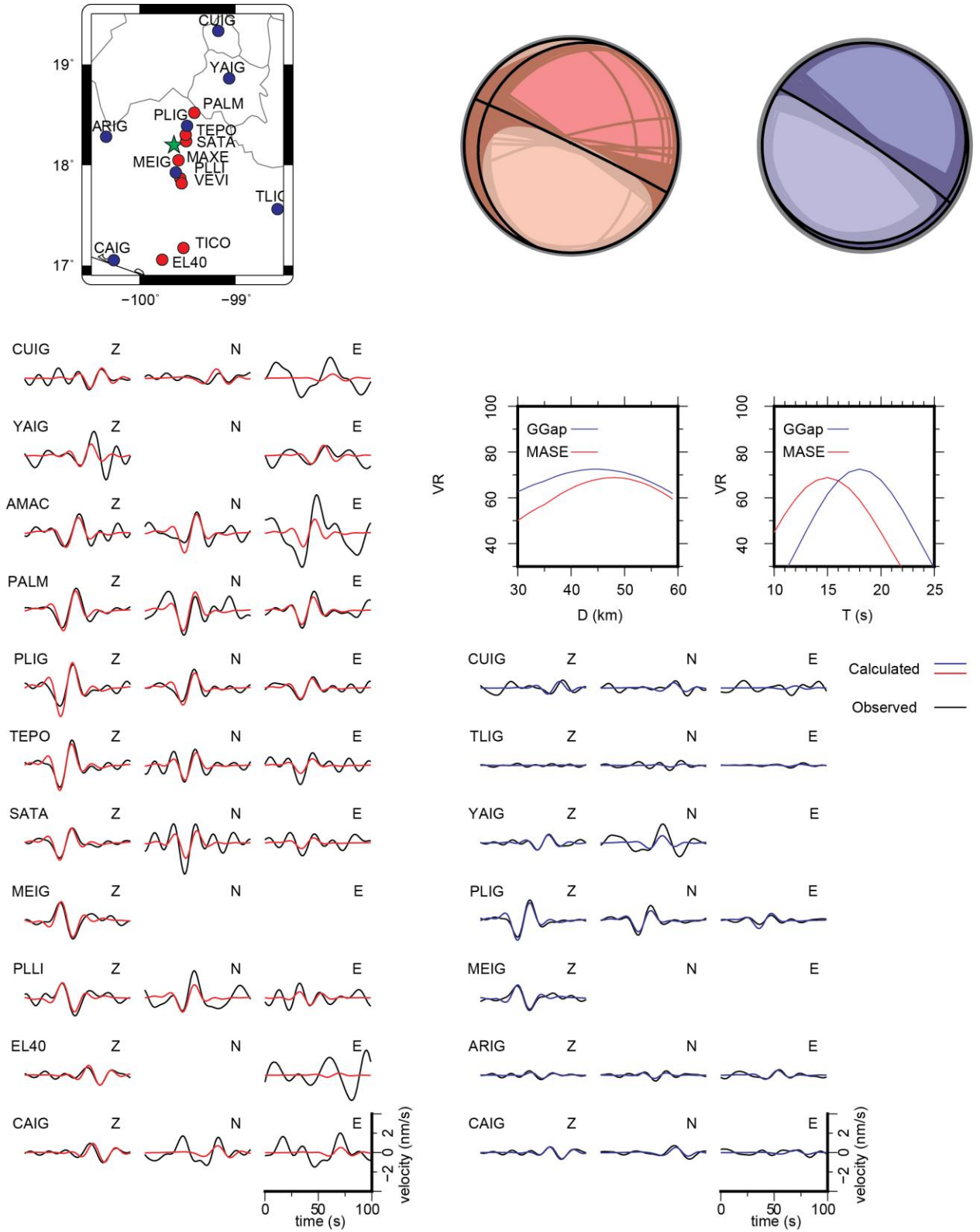
666 **Figure 3.** Standard deviations of tremor locations in the “sweet spots” region (Figure 2 **b**). The  
 667 colors indicate location errors in km. **a** and **b** are errors in latitude, **c** and **d** are errors in  
 668 longitude, and **e** and **f** are errors in depth. Upper row plots are locations of MASE data (**a**, **c**, **e**);  
 669 bottom plots are locations of G-GAP data (**b**, **d**, **f**).



670

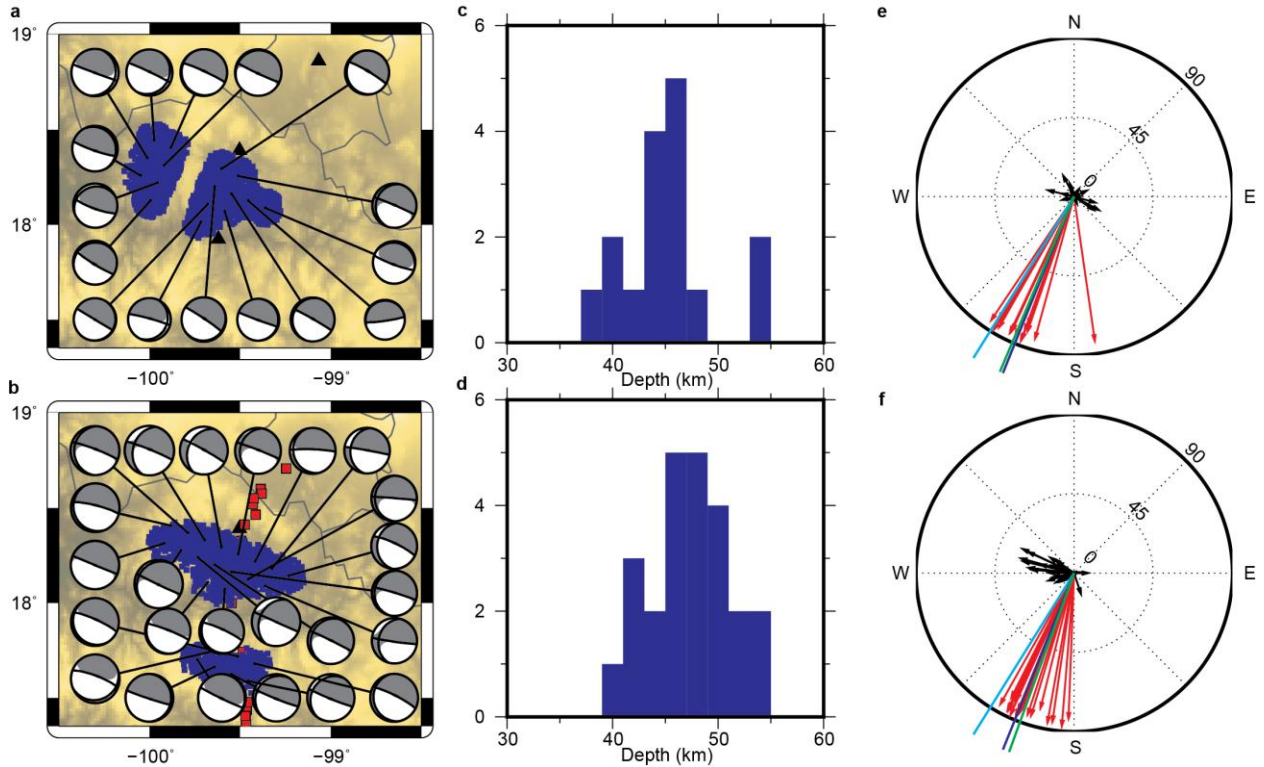
671 **Figure 4.** Maps of tremor density. The area is divided into  $2 \times 2$  km squares. Blue stars indicate  
672 locations with the highest density of tremor locations for each cluster. Black squares indicate  
673 temporary stations and triangles indicate permanent stations. **a** Density of tremor centroids  
674 during the MASE time period. **b** Tremor centroid density during the G-GAP time period. The

675 black contour indicates the 70% tremor activity limit, and the white contour indicates the 50%  
 676 tremor activity limit.



677

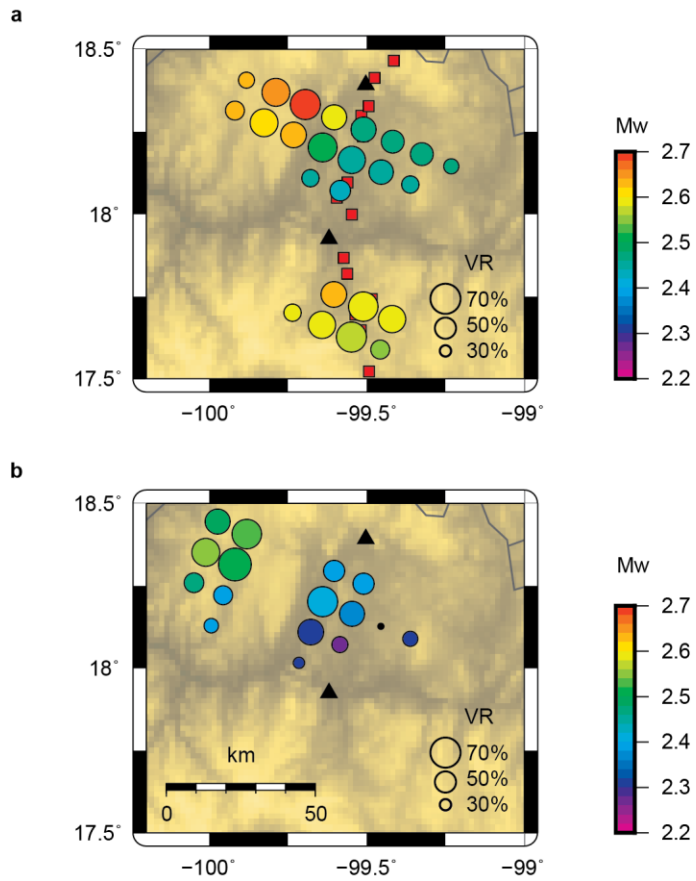
678 **Figure 5.** Sample moment tensor inversion for the grid point  $18.2^{\circ}$  N,  $-99.6^{\circ}$  W for both time  
 679 periods. Top left: map view showing the location of the grid point (green star) and stations  
 680 considered (circles). Top right: beach ball representations of the focal mechanism for the MASE  
 681 time period (red) and G-GAP time period (blue). Center right: Dependence of variance reduction  
 682 (VR) on depth and duration. Bottom: comparison between stacked and calculated (black)  
 683 waveforms. Waveforms are only shown for components with a non-null weight.



684

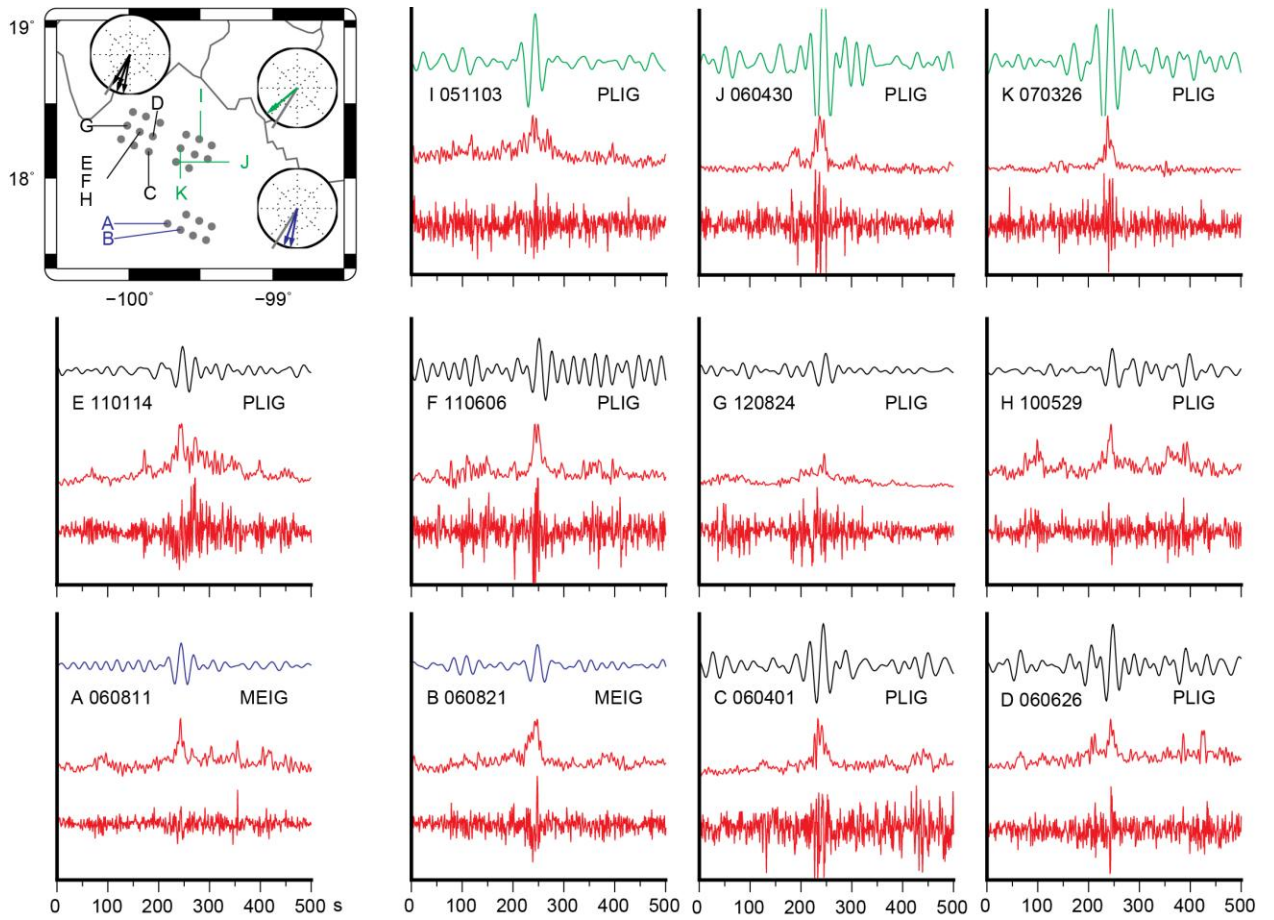
685 **Figure 6.** Full results of moment tensor inversions. The upper panel shows G-GAP results and  
 686 the lower panel shows MASE results. **a, b** Beach ball representations of focal mechanisms. **c, d**  
 687 Histograms of VLF events depths. **e, f** Directions of slip vectors (red) and fault normals (black)

688 are shown as arrows. Green lines show the mean slip direction for each dataset, blue lines show  
689 plate convergence direction, and cyan lines show dip direction.



690

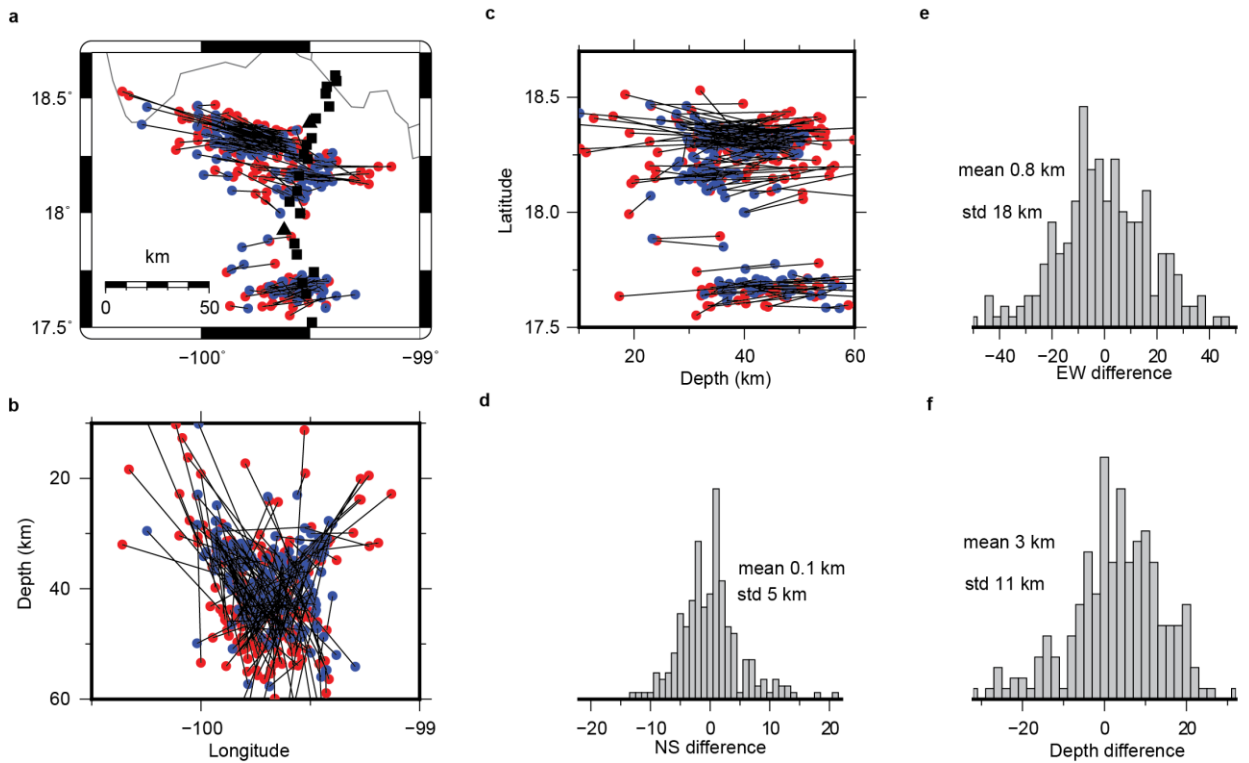
691 **Figure 7.** Magnitudes of stacked VLF events, estimated from moment tensor inversion. Size  
 692 indicate the VR value. **a** Magnitudes of events detected with MASE stations. **b** Magnitudes of  
 693 events detected with G-GAP stations.



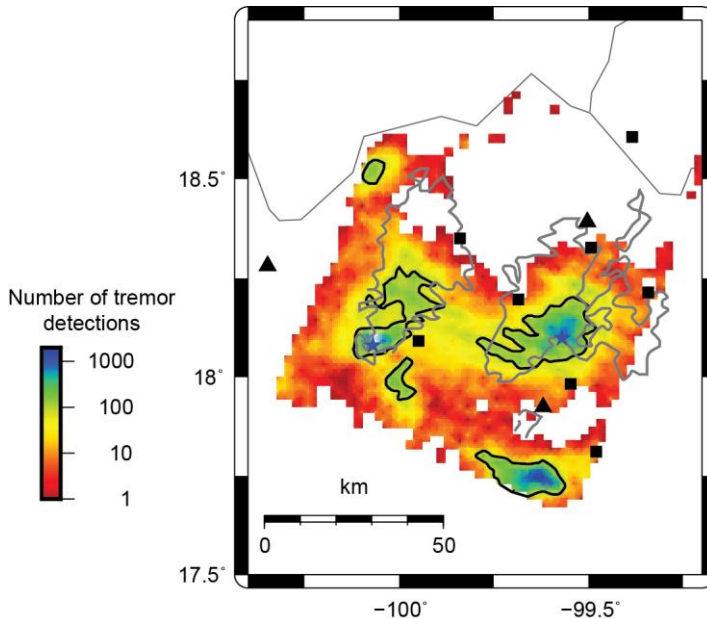
694  
 695 **Figure 8.** Results of VLF signal detection. Top left: slip direction for each cluster. The points  
 696 used in the grid search are shown as grey dots. Center: waveform for each event. The red signal  
 697 is filtered between 2 and 8 Hz, and the corresponding red envelope is shown above it. The blue,  
 698 black, and green signals show the VLF component. Blue traces correspond to the transient zone



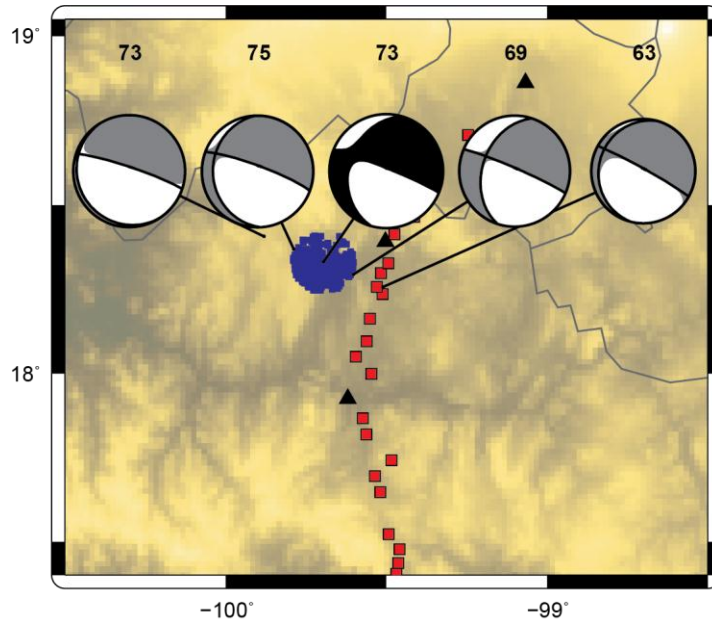
699 cluster, black to the western sweet spot, and green to the eastern sweet spot. Data from station  
 700 PLIG are shown for the sweet spots and data from MEIG are shown for the transient cluster.



701  
 702 **Figure 9.** Comparison between tremor hypocenters detected using both horizontal component  
 703 data (blue circles) and vertical component data (red circles). **a** Map view of tremor locations.  
 704 Locations of each event using horizontal and vertical component data are connected by black  
 705 lines. **b** E–W cross-section. **c** N–S cross-section. **d–f** Histograms of location latitude, longitude,  
 706 and depth.



708 **Figure 10.** Locations of tremors obtained with the TREP method. Colors represent the number of  
709 tremors within  $2 \times 2$  km bins. Black contours indicate the 70% tremor activity limit. The blue  
710 stars indicate the locations with the highest density of tremors for each cluster. Grey contours  
711 indicate the corresponding activity limits estimated using the envelope correlation method.



712

713 **Figure 11.** Moment tensor inversions for the stacked tremors located at grid point 18.3° N,  
714 -99.7° W, as a function of longitude. The black focal mechanism indicates the result for the grid  
715 point where the tremors were located. Each focal mechanism is labeled with its variance  
716 reduction.